Impact of nitrogen doping on the band structure and the charge carrier scattering in monolayer graphene

Marie-Luise Braatz,[1,2] Lothar Veith,[3] Janis Köster,[4] Ute Kaiser,[4] Axel Binder,[5] Martin Gradhand,[1,6] and Mathias Kläui[1,2]

[1]*Institute of Physics, Johannes Gutenberg University Mainz, Staudingerweg 7, 55128 Mainz, Germany*

[2]*Graduate School of Excellence Materials Science in Mainz, Staudingerweg 9, 55128 Mainz, Germany*

[3]*Max Planck Institute for Polymer Research, Ackermannweg 10, 55128 Mainz, Germany*

[4]*Electron Microscopy Group of Materials Science, Ulm University, Albert-Einstein-Allee 11, 89081 Ulm, Germany*

[5]*BASF SE, Carl-Bosch-Straße 38, 67056 Ludwigshafen, Germany*

[6]*H. H. Wills Physics Laboratory, University of Bristol, Tyndall Ave, BS8-1TL, United Kingdom*

(Received 5 February 2021; revised 9 June 2021; accepted 12 July 2021; published 12 August 2021)

The addition of nitrogen as a dopant in monolayer graphene is a flexible approach to tune the electronic properties of graphene as required for applications. Here, we investigate the impact of the doping process that adds N dopants and defects on the key electronic properties, such as the mobility, the effective mass, the Berry phase, and the scattering times of the charge carriers. Measurements at low temperatures and magnetic fields up to 9 T show a decrease of the mobility with increasing defect density due to elastic, short-range scattering. At low magnetic fields weak localization indicates an inelastic contribution depending on both defects and dopants. Analysis of the effective mass shows that the N dopants decrease the slope of the linear bands, which are characteristic for the band structure of graphene around the Dirac point. The Berry phase, however, remains unaffected by the modifications induced through defects and dopants, showing that the overall band structure of the samples is still exhibiting the key properties as expected for Dirac fermions in graphene.

DOI: 10.1103/PhysRevMaterials.5.084003

I. INTRODUCTION

Doping graphene has become a well-established route to tailoring the material properties to the respective applications. First experiments using mainly nitrogen and boron [1,2] that started soon after the first experimental studies of pristine graphene [3,4] have showcased the extraordinary properties of graphene. Now the range of heteroatoms, both in theory and applications, has increased including among others phosphorus [5], sulfur [6], fluoride [7], and potassium [8]. Choosing nitrogen as a dopant has proven to be very useful for devices in fields, such as biosensing [9,10], batteries [11], catalysis [12], and more. Additionally, doping graphene can be used as a means to gain further insights into basic physical processes taking place in graphene. With exceptionally high levels of doping it is for instance possible to reach states beyond the van Hove singularity [13] to explore whether exotic ground states are stable under these conditions. But, already for lower doping concentrations, changes in the band structure have been predicted [2,14].

Other electronic properties of interest in the context of doping graphene are scattering mechanisms of the charge carriers and the emergence of an electronic band gap, which in turn is crucial for applications in transistor devices and for spin transport properties. However, other lattice modifications such as defects or deformations can also influence the observations made on doped graphene. These include for example holes, grain boundaries, and strain. Another relevant effect is the unintentional adsorption of atoms and molecules from the air [15]. While many of these effects occur simultaneously as the doping processes introduce defects at the same time, the effects have not been clearly separated in terms of their impact on the electronic properties of doped graphene.

Here, we compare graphene samples with different levels of nitrogen doping up to 1%. Additionally, the doping process induces defects so we characterize the individual contributions on the band structure and scattering mechanisms. The effective mass and the Berry phase serve as a measure for the band structure while the weak localization (WL) is used to quantify the scattering times. With our measurements we determine which changes in the electronic and transport properties can be ascribed to which modifications in the graphene lattice and show the importance of complementary methods sensitive to different properties and effects.

II. MATERIALS AND METHODS

The samples were prepared by chemical vapor deposition where the nitrogen was incorporated into the lattice by varying the amounts of NH_3 in comparison to the other precursors (H_2, CH_4) during the growth process [16] (see Supplemental Material for more details [17]). These differences in the amount of nitrogen, small variations of the pressure and temperature during growth, and possibly inhomogeneities of the copper substrate lead to comparable samples with small variations regarding dopants and defects. The single-shot high-resolution transmission electron

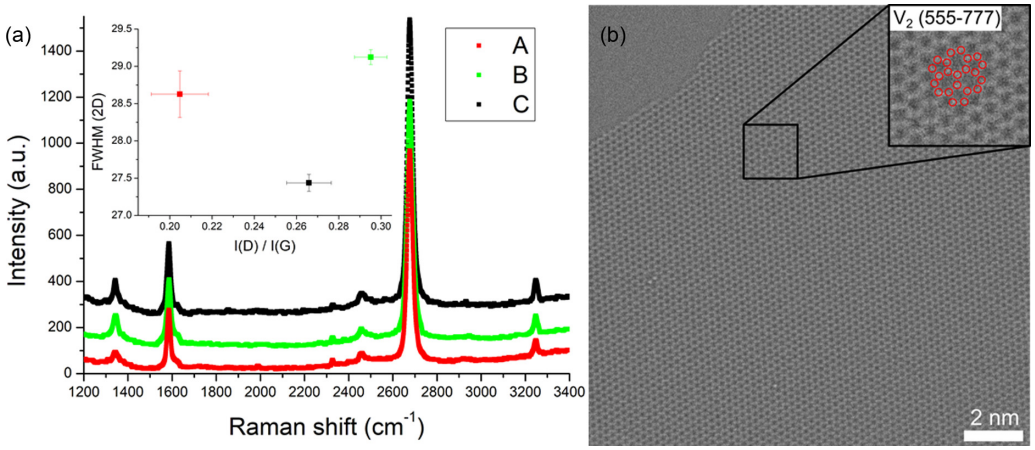

FIG. 1. Comparison of the graphene samples with different levels of nitrogen doping. (a) Raman spectra (532 nm), offset for clarity. Inset: Average of the FWHM measured on different spots of the sample and the ratio of *D*-peak intensity to *G*-peak intensity. (b) 80-kV Cc/Cs-corrected high-resolution TEM image with bright atom contrast of sample C magnified is a V_2 (555-777) [23] divacancy marked by red circles.

microscopy (TEM) image was acquired at the Cc/Cs-corrected Sub-Angström Low-Voltage Electron microscope at an acceleration voltage of 80 kV. X-ray photoelectron spectroscopy (XPS) was performed at room temperature with a Kratos Axis Ultra DLD with a spot size of approximately 300 $\times$ 700 μm and 20 spots measured per sample. For analysis a Voigt function and a Shirley background correction were used. For time-of-flight secondary ion mass spectrometry (ToF-SIMS) an IONTOF TOF.SIMS^5 NCS was used with Bi_3 at 30 keV as primary ions. Normalization of the results to the total ion count was performed to ensure comparability of the samples. The transfer followed the standard procedure of capping the graphene with polymethyl methacrylate, etching the copper by ammonium persulfate (3%), replacing it with water, and transferring the graphene onto *p*-doped Si covered with 300-nm SiO_2 [18]. Raman measurements were performed at room temperature with a 532-nm excitation laser. For the magnetoresistance measurements the samples were contacted with silver paste in four-probe geometry. The measurements were performed in vacuum in a helium cryostat with temperatures down to 3 K. The magnetic fields of up to 9 T were applied perpendicular to the sample surface.

III. RESULTS AND DISCUSSION

A. Characterization of doping level and defects

The first step is to characterize the structure and doping level of the samples for which we apply selected methods. To check the structural quality, we first employ Raman spectroscopy, which shows the characteristic peaks for graphene [Fig. 1(a), offset introduced for clarity] for the three samples we investigated (labeled A, B, and C). For all samples, the graphene is determined to be monolayer by the symmetric single-peak shape of the two-dimensional (2D) peak [19,20] (at $\sim$2679 cm^{-1}) and the intensity ratio of 2D and *G* peak (at $\sim$2679 cm^{-1}) which is larger than 2 [21]. The position of the 2D- and the *G* peak is used to demonstrate that there is no significant strain present in the samples [22] (see Supplemental Material for more details). The good quality of the monolayers is confirmed by transmission electron microscopy (TEM). An exemplary image of sample C shows the individual atoms in the lattice where a defect corresponding to two missing carbon atoms [23] can easily be identified [Fig. 1(b)].

Next, we need to quantify the doping level of our samples. From XPS we can evaluate the nitrogen concentration to be at 0.23% for sample A, 0.74% for sample B, and 1.02% for sample C (Table I). Via ToF-SIMS measurements we verify the observed trends in the doping levels. These measurements were performed on the graphene samples on the copper substrates (as grown) at 500 °C to avoid contamination by adsorbates from air. Having established the N-doping levels, we finally also need to understand the concentration of the defects. While they could also be induced by the N doping, they do not have to be directly proportional to the nitrogen concentration as the growth conditions vary. An example of a defect not directly related to the incorporation of dopants can be seen in Fig. 1(b). Detailed Raman-analysis allows us to investigate the amount of defects present in the samples. The full width at half maximum (FWHM) of the 2D peak. which has been shown to scale with the amount of defects present in the sample [24,25], is highest for sample B [Fig. 1(a), inset]. Another measure of defects is the intensity of the *D* peak [26–28]. The ratio of the intensity of the *D*- and the *G* peak is also highest for this sample [Fig. 1(a), inset], confirming the high defect density of sample B. The higher $I(D)/I(G)$ value for sample C compared to sample A is likely due to the fact that the higher doping level in sample C increases the *D*-peak

TABLE I. Overview of the samples investigated including concentration of nitrogen dopants, ratio of hole- and electron mobility (μ_h and μ_e), and qualitative defect concentration.

Sample	N concentration	μ_h/μ_e	Defect concentration
A	0.23%	1.8	Lower
B	0.74%	2.7	High
C	1.02%	1.5	Lowest

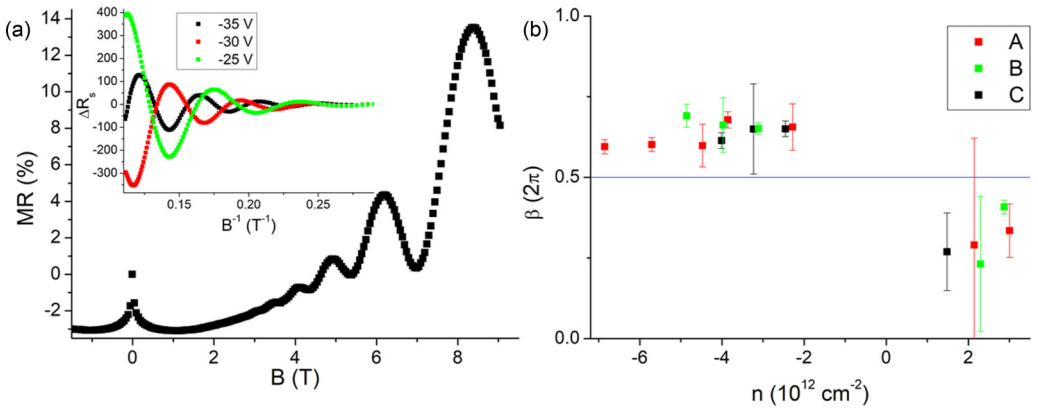

FIG. 2. (a) Magnetoresistance as a function of the magnetic field at 3 K for the sample A at $\Delta V_g = -35$ V. Inset: Subtraction of the parabolic background at different gate voltages (all hole transport side) shows clear Shubnikov–de Haas oscillations. (b) Berry phase at different charge carrier densities for different levels of N doping.

intensity even though the defect density is slightly higher for sample A. Contributions from defects and dopants can only be disentangled relatively reliably by taking into account further measurement techniques such as XPS as shown here to establish the doping level.

B. Berry phase and effective mass of the charge carriers

To relate the electrical properties and in particular the band structure to the differences found in the structure of the samples, we first study the magnetoresistance (MR) at various temperatures and gate voltages. The sheet resistance exhibits clear Shubnikov–de Haas oscillations [29] at high magnetic fields up to 9 T and up to 50 K [Fig. 2(a)]. These oscillations occur when the position of the Landau levels changes relative to the Fermi energy through the presence of a magnetic field perpendicular to the sample. The distinct oscillations confirm the overall good quality of the graphene since they would smear out otherwise and become indistinguishable.

To check for the typical electronic properties of graphene, namely the linear dispersion relation with a zero band gap and vanishing mass at the Dirac point, we take a closer look at the Berry phase β [Fig. 2(b)]. By subtracting the parabolic background [Fig. 2(a), inset] the Berry phase can be extracted from the positions of the resistance oscillations in the magnetic field via a Landau fan diagram. While materials like two-dimensional electron gases (2DEGs) or even bilayer graphene exhibit a trivial Berry phase of 0 or 1 in units of 2π, graphene, due to its peculiar band structure, has a nontrivial Berry phase of 0.5. Here we show that it holds true independent of charge carrier density, doping level, and amount of defects, so no sizable band gap is opened by either of these modifications within the experimental limits explored here. While calculations have shown gaps for different dopants, they are based on smaller unit cells equaling higher doping levels [14,30,31]. A key finding of these results is that to enable the application of doped graphene in transistor or other devices that require a band gap, one would need to explore a higher doping regime.

Having established that we have Dirac fermion-type charge carriers in all our samples, we proceed with the analysis of the band structure by taking a closer look at the effective mass of the charge carriers for the differently doped samples. By fitting the temperature dependence of the amplitude of the Shubnikov–de Haas oscillations ΔR with the Lifshitz-Kosevich theory [32,33], the cyclotron mass m^* of the charge carriers can be extracted from $\Delta R \propto \chi/\sinh\chi$ with $\chi = (2\pi^2 k T m^*)/(\hbar e B)$ as shown in Fig. 3. For graphene the cyclotron mass, as extracted by this measurement, and the effective mass are equivalent [34], which does allow us to compare the obtained values to theory and other experimental data. Looking at the individual samples, the values follow the theoretical prediction of $m^* = (\hbar/v_F)\sqrt{\pi n}$, indicating that the bands dominating the transport are indeed linear in k space for the energy region probed as inferred from the calculation of the Berry phase [33,35]. The Fermi velocity v_F, the proportionality factor and only fitting parameter in Fig. 3, is found to be between 1.2×10^6 m/s (sample C—high doping) and 1.4×10^6 m/s (sample A—low doping). Both Fermi velocity and effective mass are also in good agreement with what has previously been measured for monolayer graphene: for very small charge carrier densities, the effective mass has been shown to be as small as $0.01\,m_e$ [36] while for comparable and slightly larger charge carrier densities it has been measured to be between 0.035 and $0.04\,m_e$ [35]. Comparing now the differently doped samples, one notes that the effective

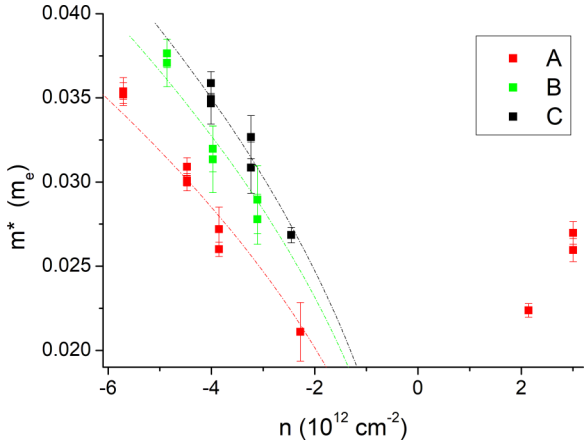

FIG. 3. Effective mass of the charge carriers at different charge carrier densities for different levels of N doping with fit of $m^* \propto \sqrt{n}$.

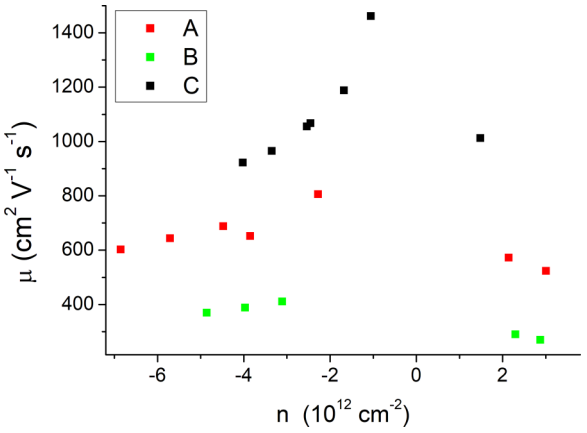

FIG. 4. Charge carrier mobility from Hall measurements as a function of charge carrier density at 3 K for different levels of N doping.

mass depends mainly on the amount of nitrogen and not on the amount of defects. This leads to the conclusion that the dopants, which add further charge carriers to the system, influence the band structure more strongly than the defects. While the linear bands are preserved, the slope of these bands is reduced by larger concentrations of nitrogen. The additional N atoms are thus reducing the Fermi velocity of the charge carriers.

C. Charge carrier mobility

Having established the electronic properties, our next step is to check the effect of the doping on the charge transport properties and especially the different scattering mechanisms of the charge carriers. We compare the charge carrier mobility of the different samples extracted by two different methods at different gate voltages and temperatures. We see a clear inverse correlation of mobility and the defect density: sample B exhibits a significantly lower mobility than the other two samples while having a higher defect density (Fig. 4). Both Hall measurements as well as back-gate sweeps show that this relation holds true over the whole charge carrier density- and temperature range (see Supplemental Material for more details). The observed decrease of mobility with increasing charge carrier concentration can be fitted well with a $1/n$ dependence. This is typical for short-range scattering which is mostly caused by vacancies, dislocations, or other neutral defects [37]. Furthermore, the asymmetry between the mobility of the electrons and holes, which has been shown to correlate with the amount of defects [38], is also increased for sample B (Table I). The ratio of hole and electron mobility is 2.7 for sample B, yet only 1.8 and 1.5 for samples A and C, respectively, confirming a lower defect density in these samples.

D. Phase coherence and scattering times

As highlighted so far, our N-doped graphene samples exhibit the characteristics of the linear dispersion, including the vanishing effective mass, the divergence of the mobility, as well as the nontrivial phase arising from the physics at the Dirac points. All those results compare well with the existing literature [35,39], broadening the scope concerning the different effects of doping and defects and are internally consistent albeit only weakly dependent on the N-doping level. Only for the effective mass a correlation between the N-doping concentration was visible with a higher doping leading to a reduction of the Fermi velocity. In contrast, the Berry phase was neither affected by the doping nor in fact other defects across the samples pointing to the similarity across the samples with marginal effects on the induced gap around the Dirac point. On the other hand, the mobility was clearly correlated with the defect level related to the purity of the samples beyond the N doping.

To better understand the different scattering mechanisms playing the dominant role in our samples, we analyze the MR at low magnetic fields. As has been shown previously [40], localized N substitutional impurities predominantly serve as elastic intervalley scatterers where the scattering rate should scale with the impurity concentration. At the same time this contribution was argued to depend on temperature only weakly, while the phase relaxation time, mainly capturing inelastic processes, scales more dominantly with the temperature [41]. Here, we aim to put a similar analysis to the test for our samples which, as discussed above, show all the standard signatures of the Dirac band structure. As shown in Fig. 2(a), a clear WL peak [42] is visible in all the samples for fields below 1 T. Generally, in 2D systems, weak antilocalization would be expected due to coherent backscattering but a stronger intervalley scattering, which breaks the chiral symmetry, restores the WL [43]. We fit the magnetoresistance for fields up to 0.3 T with a model that considers the phase coherence time τ_ϕ, the intervalley scattering time τ_i, and the intravalley scattering τ_* [42]:

$$\Delta R(B) = -\frac{e^2\rho_s^2}{\pi\, h}\left[F(dB\tau_\phi) - F\left(\frac{dB}{{\tau_\phi}^{-1} + 2{\tau_i}^{-1}}\right) - 2F\left(\frac{dB}{{\tau_\phi}^{-1} + {\tau_i}^{-1} + {\tau_*}^{-1}}\right)\right],$$

with $d = (4eD/\hbar)$, D the diffusion constant, $F(z) = \ln(z) + \Psi(1/2 + 1/z)$, and $\Psi(z)$ the digamma function. The intravalley scattering time is calculated according to Moser *et al.* [44] in order to reduce the number of free parameters. This model captures the essential behavior of WL in graphene while relying only on the two parameters intervalley scattering time and phase coherence time. While the intervalley scattering time is roughly independent of temperature, the phase coherence time increases for decreasing temperatures and shows a saturation around 10 K [Fig. 5(b)] for the negative charge carrier density. This agrees well with previous reports for the general dependence and with respect to the saturation for temperatures below 10 K, which is attributed to either scattering from substrate impurities and air [45] or increased electron-electron interaction [41,46]. The different low-temperature-behavior depending on charge carrier type as highlighted in the inset indicates different scattering mechanisms on the electron and hole side of the Dirac point at low temperatures. While the parabolic behavior can be attributed to Coulomb interaction, the linear behavior is typically ascribed to inelastic Nyquist scattering [40,47]. τ_ϕ decreases slightly with the charge

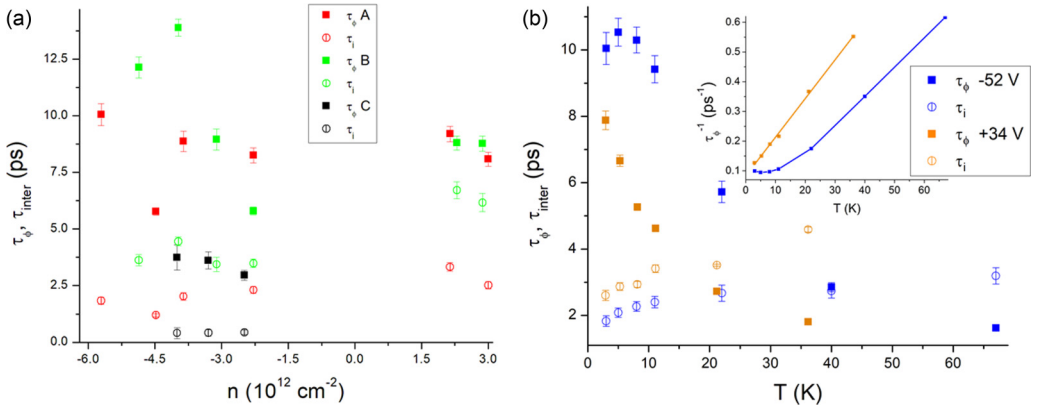

FIG. 5. Phase coherence time and intervalley scattering time (a) at different charge carrier densities for different N-doping levels corresponding to samples A, B, and C at 3 K and (b) at different temperatures at the effective gate voltage $\Delta V_g = -52$ V ($n = -5.7 \times 10^{12}$ cm^{-2}) and $+34$ V($n = 2.1 \times 10^{12}$ cm^{-2}) for sample A. Inset shows the different scaling of the phase coherence breaking rate for electron (linear) and hole (quadratic) side for this sample.

carrier density [Fig. 5(a)], which can be attributed to increased electron-hole puddles near the Dirac point [43,46]. More striking is the dependence on mobility: Both τ_ϕ and τ_i increase with decreasing mobility pointing to different mechanisms affecting mobility in contrast to the relaxation times. They are likely driven by inelastic processes while the mobility directly correlates with the defect level associated with elastic scattering. This altogether highlights the fact that the observed relaxation times do strongly depend on the exact growth and preparation conditions of the individual samples, which has led to contradictory observations in the past [48]. This work thus highlights the importance of probing all the different parameters for a given sample since distinct probes access different physics and might lead to different conclusions if not tested against each other. Further WL studies with higher resolution could enable disentangling scattering on the electron or hole side of the Dirac point, which might show a different dependence for defects and dopants. That way the reason for differences in the disorder potential could be attributed more clearly to the different types of scatterers.

IV. CONCLUSIONS

We have studied the influence of N doping and defects in graphene on both the band structure and charge carrier scattering mechanisms. Doping graphene with up to 1% nitrogen leads to a change in the slope of the linear bands but the overall band structure of Dirac fermion charge carriers is retained, as shown by the nontrivial Berry phase. The charge carrier mobility is decreased for the sample with higher defect density, which thus leads to stronger elastic, short-range scattering. The scattering times as extracted from the WL measurements are likely due to inelastic processes both from the defects and doping present in the samples. The lowest values for the scattering in sample C could be due to scattering at the localized N dopants which break the phase coherence. Generally, we have shown that the band structure is overall robust to these perturbations generated by the N doping and the defects and no significant transport gap is opened for either of the samples. To achieve substantial band-structure modifications the amount of doping could be increased or the type of dopant varied.

ACKNOWLEDGMENTS

M.-L.B. thanks Libor Smejkal and Thomas Gauntlett Saunderson for stimulating discussions on the band structure and Berry phase, Leon Prädel for XPS measurements, and Nils-Eike Weber for developing experimental procedures for preparing doped graphene. M.G. acknowledges the visiting professorship program of the Centre for Dynamics and Topology and Johannes Gutenberg-University Mainz. This work was financially supported by the DFG primarily through the Priority Program Graphene SPP 1459 (Grant No. 130170629), SFB TRR 173 Spin + X, Projects A01 and B02 (Grant 268565370), and the Forschungsinitiative Rheinland-Pfalz through the Center for Dynamics and Topology (TopDyn).

[1] F. Joucken, L. Henrard, and J. Lagoute, Electronic properties of chemically doped graphene, Phys. Rev. Materials **3**, 110301 (2019).

[2] L. S. Panchakarla, K. S. Subrahmanyam, S. K. Saha, A. Govindaraj, H. R. Krishnamurthy, U. V. Waghmare, and C. N. R. Rao, Synthesis, structure, and properties of boron- and nitrogen-doped graphene, Adv. Mater. **21**, 4726 (2009).

[3] A. K. Geim, Graphene: Status and prospects, Science **324**, 1530 (2009).

[4] A. H. Castro Neto, F. Guinea, N. M. R. Peres, K. S. Novoselov, and A. K. Geim, The electronic properties of graphene, Rev. Mod. Phys. **81**, 109 (2009).

[5] Y. Wen, B. Wang, C. Huang, L. Wang, and D. Hulicova-Jurcakova, Synthesis of phosphorus-doped graphene and its

wide potential window in aqueous supercapacitors, Chem.–Eur. J. **21**, 80 (2015).

[6] Z. Yang, Z. Yao, G. Li, G. Fang, H. Nie, Z. Liu, X. Zhou, X. Chen, and S. Huang, Sulfur-doped graphene as an efficient metal-free cathode catalyst for oxygen reduction, ACS Nano **6**, 205 (2012).

[7] K. Kakaei and A. Balavandi, Hierarchically porous fluorine-doped graphene nanosheets as efficient metal-free electrocatalyst for oxygen reduction in gas diffusion electrode, J. Colloid Interface Sci. **490**, 819 (2017).

[8] C. A. Howard, M. P. M. Dean, and F. Withers, Phonons in potassium-doped graphene: The effects of electron-phonon interactions, dimensionality, and adatom ordering, Phys. Rev. B **84**, 241404(R) (2011).

[9] Y. Wang, Y. Shao, D. W. Matson, J. Li, and Y. Lin, Nitrogen-doped graphene and its application in electrochemical biosensing, ACS Nano **4**, 1790 (2010).

[10] S. Kaushal, M. Kaur, N. Kaur, V. Kumari, and P. Pal Singh, Heteroatom-doped graphene as sensing materials: A mini review, RSC Adv. **10**, 28608 (2020).

[11] A. L. M. Reddy, A. Srivastava, S. R. Gowda, H. Gullapalli, M. Dubey, and P. M. Ajayan, Synthesis Of nitrogen-doped graphene films for lithium battery application, ACS Nano **4**, 6337 (2010).

[12] Y. Wang, Y. Shen, Y. Zhou, Z. Xue, Z. Xi, and S. Zhu, Heteroatom-doped graphene for efficient no decomposition by metal-free catalysis, ACS Appl. Mater. Interfaces **10**, 36202 (2018).

[13] P. Rosenzweig, H. Karakachian, D. Marchenko, K. Küster, and U. Starke, Overdoping Graphene Beyond the van Hove Singularity, Phys. Rev. Lett. **125**, 176403 (2020).

[14] P. Rani and V. K. Jindal, Designing band gap of graphene by B and N dopant atoms, RSC Adv. **3**, 802 (2013).

[15] H. I. Wang, M.-L. Braatz, N. Richter, K.-J. Tielrooij, Z. Mics, H. Lu, N.-E. Weber, K. Müllen, D. Turchinovich, M. Kläui, and M. Bonn, Reversible photochemical control of doping levels in supported graphene, J. Phys. Chem. C **121**, 4083 (2017).

[16] Y. Ito, C. Christodoulou, M. V. Nardi, N. Koch, H. Sachdev, and K. Müllen, Chemical vapor deposition of n-doped graphene and carbon films: The role of precursors and gas phase, ACS Nano **8**, 3337 (2014).

[17] See Supplemental Material at http://link.aps.org/supplemental/10.1103/PhysRevMaterials.5.084003 for details on growth conditions, strain in graphene, and the temperature dependence of the mobility.

[18] M. Rein, N. Richter, K. Parvez, X. Feng, H. Sachdev, M. Kläui, and K. Müllen, Magnetoresistance and charge transport in graphene governed by nitrogen dopants, ACS Nano **9**, 1360 (2015).

[19] A. C. Ferrari, J. C. Meyer, V. Scardaci, C. Casiraghi, M. Lazzeri, F. Mauri, S. Piscanec, D. Jiang, K. S. Novoselov, S. Roth, and A. K. Geim, Raman Spectrum of Graphene and Graphene Layers, Phys. Rev. Lett. **97**, 187401 (2006).

[20] L. M. Malard, M. A. Pimenta, G. Dresselhaus, and M. S. Dresselhaus, Raman spectroscopy in graphene, Phys. Rep. **473**, 51 (2009).

[21] G. S. Papanai, I. Sharma, and B. K. Gupta, Probing number of layers and quality assessment of mechanically exfoliated graphene via Raman fingerprint, Mater. Today Commun. **22**, 100795 (2020).

[22] J. E. Lee, G. Ahn, J. Shim, Y. S. Lee, and S. Ryu, Optical separation of mechanical strain from charge doping in graphene, Nat. Commun. **3**, 1024 (2012).

[23] J. Kotakoski, A. V. Krasheninnikov, U. Kaiser, and J. C. Meyer, From Point Defects in Graphene to Two-Dimensional Amorphous Carbon, Phys. Rev. Lett. **106**, 105505 (2011).

[24] E. H. Martins Ferreira, M. V. O. Moutinho, F. Stavale, M. M. Lucchese, R. B. Capaz, C. A. Achete, and A. Jorio, Evolution of the Raman spectra from single-, few-, and many-layer graphene with increasing disorder, Phys. Rev. B **82**, 125429 (2010).

[25] C. Neumann, S. Reichardt, P. Venezuela, M. Drögeler, L. Banszerus, M. Schmitz, K. Watanabe, T. Taniguchi, F. Mauri, B. Beschoten, S. V. Rotkin, and C. Stampfer, Raman spectroscopy as probe of nanometre-scale strain variations in graphene, Nat. Commun. **6**, 8429 (2015).

[26] Z. Zafar, Z. H. Ni, X. Wu, Z. X. Shi, H. Y. Nan, J. Bai, and L. T. Sun, Evolution of Raman spectra in nitrogen doped graphene, Carbon **61**, 57 (2013).

[27] F. Tuinstra and J. L. Koenig, Raman spectrum of graphite, J. Chem. Phys. **53**, 1126 (1970).

[28] M. M. Lucchese, F. Stavale, E. H. M. Ferreira, C. Vilani, M. V. O. Moutinho, R. B. Capaz, C. A. Achete, and A. Jorio, Quantifying ion-induced defects and Raman relaxation length in graphene, Carbon **48**, 1592 (2010).

[29] Z. Tan, C. Tan, L. Ma, G. T. Liu, L. Lu, and C. L. Yang, Shubnikov-de Haas oscillations of a single layer graphene under dc current bias, Phys. Rev. B **84**, 115429 (2011).

[30] K. Iyakutti, E. M. Kumar, I. Lakshmi, R. Thapa, R. Rajeswarapalanichamy, V. J. Surya, and Y. Kawazoe, Effect of surface doping on the band structure of graphene: A DFT Study, J. Mater. Sci. Mater. Electron. **27**, 2728 (2016).

[31] J. Lee, S. Kwon, S. Kwon, M. Cho, K. Kim, T. Han, and S. Lee, Tunable electronic properties of nitrogen and sulfur doped graphene: Density functional theory approach, Nanomaterials **9**, 268 (2019).

[32] I. M. Lifshitz and A. M. Kosevich, On the theory of magnetic susceptibility of metals at low temperatures, Zh. Eksp. Theor. Fiz. **29**, 730 (1955) [Sov. Phys. JETP **2**, 636 (1956)]

[33] Y. Cao, V. Fatemi, A. Demir, S. Fang, S. L. Tomarken, J. Y. Luo, J. D. Sanchez-Yamagishi, K. Watanabe, T. Taniguchi, E. Kaxiras, R. C. Ashoori, and P. Jarillo-Herrero, Correlated insulator behaviour at half-filling in magic-angle graphene superlattices, Nature (London) **556**, 80 (2018).

[34] V. Ariel and A. Natan, Electron Effective Mass in Graphene, in *Proceedings of the 2013 International Conference on Electromagnetics in Advanced Applications (ICEAA), Turin, Italy* (IEEE, 2013), pp. 696–698.

[35] Y. Zhang, Y.-W. Tan, H. L. Stormer, and P. Kim, Experimental observation of the quantum Hall effect and Berry's phase in graphene, Nature (London) **438**, 201 (2005).

[36] E. Tiras, S. Ardali, T. Tiras, E. Arslan, S. Cakmakyapan, O. Kazar, J. Hassan, E. Janzén, and E. Ozbay, Effective mass of electron in monolayer graphene: Electron-phonon interaction, J. Appl. Phys. **113**, 043708 (2013).

[37] E. Zion, A. Butenko, A. Sharoni, M. Kaveh, and I. Shlimak, Charge carrier transport asymmetry in monolayer graphene, Phys. Rev. B **96**, 245143 (2017).

[38] K.-K. Bai, Y.-C. Wei, J.-B. Qiao, S.-Y. Li, L.-J. Yin, W. Yan, J.-C. Nie, and L. He, Detecting giant electron-hole asymmetry in a graphene monolayer generated by strain and charged-defect scattering via Landau level spectroscopy, Phys. Rev. B **92**, 121405(R) (2015).

[39] D. R. Cooper, B. D'Anjou, N. Ghattamaneni, B. Harack, M. Hilke, A. Horth, N. Majlis, M. Massicotte, L. Vandsburger, E. Whiteway, and V. Yu, Experimental review of graphene, ISRN Condens. Matter Phys. **2012**, 501686 (2012).

[40] J. Li, L. Lin, D. Rui, Q. Li, J. Zhang, N. Kang, Y. Zhang, H. Peng, Z. Liu, and H. Q. Xu, Electron–hole symmetry breaking in charge transport in nitrogen-doped graphene, ACS Nano **11**, 4641 (2017).

[41] F. V. Tikhonenko, D. W. Horsell, R. V. Gorbachev, and A. K. Savchenko, Weak Localization in Graphene Flakes, Phys. Rev. Lett. **100**, 056802 (2008).

[42] E. McCann, K. Kechedzhi, V. I. Fal'ko, H. Suzuura, T. Ando, and B. L. Altshuler, Weak-Localization Magnetoresistance and Valley Symmetry in Graphene, Phys. Rev. Lett. **97**, 146805 (2006).

[43] D.-K. Ki, D. Jeong, J.-H. Choi, H.-J. Lee, and K.-S. Park, Inelastic scattering in a monolayer graphene sheet: A weak-localization study, Phys. Rev. B **78**, 125409 (2008).

[44] J. Moser, H. Tao, S. Roche, F. Alzina, C. M. Sotomayor Torres, and A. Bachtold, Magnetotransport in disordered graphene exposed to ozone: From weak to strong localization, Phys. Rev. B **81**, 205445 (2010).

[45] C. Chuang, L.-H. Lin, N. Aoki, T. Ouchi, A. M. Mahjoub, T.-P. Woo, R. K. Puddy, Y. Ochiai, C. G. Smith, and C.-T. Liang, Mesoscopic conductance fluctuations in multi-layer graphene, Appl. Phys. Lett. **103**, 043117 (2013).

[46] S. V. Morozov, K. S. Novoselov, M. I. Katsnelson, F. Schedin, L. A. Ponomarenko, D. Jiang, and A. K. Geim, Strong Suppression of Weak Localization in Graphene, Phys. Rev. Lett. **97**, 016801 (2006).

[47] X. C. Yang, H. M. Wang, T. R. Wu, F. Q. Huang, J. Chen, X. X. Kang, Z. Jin, X. M. Xie, and M. H. Jiang, Magnetotransport of polycrystalline graphene: Shubnikov-de Haas oscillation and weak localization study, Appl. Phys. Lett. **102**, 233503 (2013).

[48] X. Wu, X. Li, Z. Song, C. Berger, and W. A. de Heer, Weak Antilocalization in Epitaxial Graphene: Evidence for Chiral Electrons, Phys. Rev. Lett. **98**, 136801 (2007).